Available online at www.sciencedirect.com
ScienceDirect
Acta Materialia 56 (2008) 1785–1796
Acta MATERIALIA
www.elsevier.com/locate/actamat

Zr–(Cu,Ag)–Al bulk metallic glasses

Q.K. Jiang [a], X.D. Wang [a], X.P. Nie [a], G.Q. Zhang [b], H. Ma [c], H.-J. Fecht [c,d], J. Bendnarcik [e], H. Franz [e], Y.G. Liu [f], Q.P. Cao [a], J.Z. Jiang [a,*]

[a] International Center for New-Structured Materials (ICNSM), Zhejiang University and Laboratory of New-Structured Materials, Department of Materials Science and Engineering, Zhejiang University, Hangzhou 310027, China
[b] Key Laboratory of Advanced Textile Materials and Manufacturing Technology, Zhejiang Sci-Tech University, Hangzhou 310018, PR China
[c] Department of Materials, Faculty of Engineering, University of Ulm, Albert-Einstein Allee 47, D-89081 Ulm, Germany
[d] Forschungszentrum Karlsruhe, Institut für Nanotechnologie, Karlsruhe, Germany
[e] HASYLAB am DESY, Notkestrasse 85, D-22603 Hamburg, Germany
[f] Institute of Geochemistry, Chinese Academy of Sciences, Guiyang 550002, PR China

Received 12 October 2007; received in revised form 5 December 2007; accepted 14 December 2007
Available online 12 February 2008

Abstract

In this paper, we report the formation of a series Zr–(Cu,Ag)–Al bulk metallic glasses (BMGs) with diameters at least 20 mm and demonstrate the formation of about 25 g amorphous metallic ingots in a wide Zr–(Cu,Ag)–Al composition range using a conventional arc-melting machine. The origin of high glass-forming ability (GFA) of the Zr–(Cu,Ag)–Al alloy system has been investigated from the structural, thermodynamic and kinetic points of view. The high GFA of the Zr–(Cu,Ag)–Al system is attributed to denser local atomic packing and the smaller difference in Gibbs free energy between amorphous and crystalline phases. The thermal, mechanical and corrosion properties, as well as elastic constants for the newly developed Zr–(Cu,Ag)–Al BMGs, are also presented. These newly developed Ni-free Zr–(Cu,Ag)–Al BMGs exhibit excellent combined properties: strong GFA, high strength, high compressive plasticity, cheap and non-toxic raw materials and biocompatible property, as compared with other BMGs, leading to their potential industrial applications.

Keywords: Glass-forming ability; Bulk metallic glass; Thermodynamics; Structure

1. Introduction

Bulk metallic glasses (BMGs) have been regarded as potential structural materials since their first emergence several decades ago. Great effort has been made to develop alloy systems with excellent glass-forming ability (GFA) by cooling the alloys from the liquid state to mm-sized glassy materials [1–5]. To date, great successes have been achieved in several alloy systems in terms of producing amorphous alloys with diameters larger than 20 mm in Pd [6], Zr [7], Y [8], Mg [9], and La-based alloys [10]. However, one of the drawbacks severely restricting their applications as structural materials is that glassy alloys do not simultaneously have high GFA, decent ductility, superior strength, and high fracture toughness, made with cheap and environmentally friendly raw materials.

Recently, due to their excellent mechanical properties and cheap and environmentally friendly raw materials used, bulk metallic glasses based on copper and zirconium have been paid considerable attention since binary Cu–Zr and Cu–Hf BMGs were fabricated [11–17]. Among these, the ZrCuAl and ZrCuAlM (M = Ti, Ag, etc.) BMGs free of poisonous (Be, Ni, etc.) and noble elements (Pd, Pt, etc.), exhibiting excellent glass-forming ability as well as good mechanical properties, are promising engineering materials. Very recently, we reported preliminary results on Zr–(Cu,Ag)–Al alloys, which can be successfully fabricated fully amorphous with diameters at least 20 mm [18]. However, as is proved by experiments, GFA of BMGs

* Corresponding author. Tel./fax: +86 571 87952107.
E-mail address: jiangjz@zju.edu.cn (J.Z. Jiang).

1359-6454/$34.00
doi:10.1016/j.actamat.2007.12.030

is sensitive to the alloy compositions [10,15,19,20]; for example, in the La–Al–(Cu,Ag) alloys, the Cu/Ag ratio can significantly influence their GFA. This factor has not been considered in our previous Zr–(Cu,Ag)–Al work [18]. Furthermore, the effect of Ag addition and the origin of the high glass-forming ability of the Zr–(Cu,Ag)–Al alloys are still not well understood.

In this paper, a systematic study of the Zr–(Cu,Ag)–Al alloy system has been carried out. We report the formation of a series Zr–(Cu,Ag)–Al BMGs with diameters at least 20 mm. By simultaneous refinement of the Cu/Ag ratio and relative contents of Zr and Al, we optimize the composition range for glass formation and demonstrate the formation of about 25 g amorphous metallic ingots in a wide Zr–(Cu,Ag)–Al composition range using a conventional arc-melting machine. The effect of Ag addition on GFA of the quaternary alloy is systematically investigated from the structural, thermodynamic and kinetic points of view. The high glass-forming ability in the Zr–(Cu,Ag)–Al BMG alloy system is attributed to denser local atomic packing and the smaller difference in Gibbs free energy between amorphous and crystalline phases. The thermal, mechanical and corrosion properties, as well as elastic constants for the newly developed Zr–(Cu,Ag)–Al BMGs are also presented. By comparing with other BMGs (e.g., Mg-, La-, Pd- and Y-based), these newly developed Ni-free Zr–(Cu,Ag)–Al BMGs are promising for industrial applications considering their combining properties, i.e., high GFA, high strength, high compressive plasticity, cheap and non-toxic raw materials and biocompatible property.

2. Experimental

Metallic ingots of $Zr_{100-x-y}(Cu_z\ Ag_{1-z})_yAl_x$ ($x = 7$–9 at.%, y = 38–50 at.% and z = 0.75–0.875) alloys were prepared by arc-melting a mixture of pure Cu (99.9 at.%), Zr (99.8 at.%), Al (99.99 at.%) and Ag (99.9 at.%) in a Ti-gettered argon atmosphere. Each ingot was arc-melted at least four times to achieve chemical homogeneity. The weight loss of samples by alloying was less than 0.1%. For smaller samples (diameter $\leqslant$20 mm), the master alloys were further processed by suction-casting into copper mold in a high-vacuum (2×10^{-5} torr) chamber under a purified argon atmosphere, in which 20 mm is the maximum size of copper mold for suction-casting in our laboratory. For rods with diameter of 30 mm, alloys were induction melted in a low-vacuum (2×10^{-1} torr) chamber using a BN crucible container, followed by tilt-pouring the melt into copper mold with cavity of 30 mm in diameter and 60 mm in length.

To examine the structure of the rods prepared, the transverse cross-sections of the samples were examined on a Rigaku X-ray diffractometer with Cu K_α radiation at 45 kV. The central parts of the arc-melted ingots and 20 mm cast cylindrical samples were analyzed on a NETZSCH DSC 404 C differential scanning calorimeter under a continuous argon flow at a heating rate of 20 K min^{-1}.

Structural analyses of newly developed Zr–(Cu,Ag)–Al BMGs were also conducted by using synchrotron radiation X-ray diffraction at BW5 station of HASYLAB, Hamburg [21]. The beam size was $1 \times 1\ mm^2$ and the wavelength used was 0.12398 Å. High-resolution X-ray diffraction (HRXRD) patterns for $Zr_{46}(Cu_{4.5/5.5}Ag_{1/5.5})_{46}Al_8$ BMGs with 20 mm in diameter with large q range were recorded on an image plate (MAR 345, with $150 \times 150\ \mu m^2$ pixel size). Scattering intensity $I(q)$ (versus scattering vector) were extracted by using the software package FIT2D [22]. Then, structure factor $S(q)$ and reduced radial distribution function (PDF) $G(r)$ and $g(r)$ pair correlation function are obtained by PDFgetX2 according to the following equations [23]:

$$G(r) = 4\pi r[(\rho(r) - \rho_0)] = \frac{2}{\pi}\int_0^\infty q \cdot I(q) \cdot \sin(qr)\,dq \tag{1}$$

$$g(r) = \frac{\rho(r)}{\rho_0} = 1 + \frac{G(r)}{4\pi r \rho_0} \tag{2}$$

$$S(q) = 1 + \frac{4\pi\rho_0}{q}\int_0^\infty r[g(r) - 1]\sin(qr)\,dr \tag{3}$$

where $\rho(r)$ is the radial density function, ρ_0 the average atomic number density, $S(q)$ scattering factor, $q = 4\pi\sin(\theta)/\lambda$.

To study the kinetic and thermal stability properties of the newly developed Zr–(Cu,Ag)–Al BMGs, DSC measurements with different scanning rates ($\phi = 10$, 20, 40, 80 and 120 K min^{-1}) were performed on Perkin–Elmer DSC-7. The specific heat capacities of the amorphous phase, supercooled liquid phase, and crystalline phase were also measured on DSC-7 by comparing with the specific heat capacity of a sapphire standard sample using Eq. (4) [24]:

$$C_p(T)_{\text{sample}} = \frac{\dot{Q}_{\text{sample}} - \dot{Q}_{\text{pan}}}{\dot{Q}_{\text{sample}} - \dot{Q}_{\text{pan}}} \times \frac{m_{\text{sapphire}} \times \mu_{\text{sample}}}{m_{\text{sample}} \times \mu_{\text{sapphire}}} \times C_p(T)_{\text{sapphire}} \tag{4}$$

where m is the mass, μ the molecular weight and $C_p(T)_{\text{sapphire}}$ the standard specific heat capacity of the sapphire. The term $\dot{Q}$ is defined as [24]:

$$\dot{Q} = \frac{dQ}{dt} = \left(\frac{\partial Q}{\partial t}\right)_{T\neq 0} - \left(\frac{\partial Q}{\partial t}\right)_{T=0} = C \cdot \frac{dT}{dt} \tag{5}$$

and the first term $(\partial Q/\partial t)_{T\neq 0}$ corresponds to the power necessary to heat or cool the sample and its sample pan at a constant rate of 5 K min^{-1}, $(\partial Q/\partial t)_{T=0}$ is the power needed to hold the sample and its pan isothermally and C refers to the heat capacity of the sample and the pan. In order to identify the heat flow into the sample, identical measurements were also performed on the empty sample pan and a sapphire reference. The specific heat capacity of the sample is then calculated. The heat capacity measurements were repeated at 5 K intervals using a heating rate of 5 K min^{-1}.

Vickers hardness of newly developed Zr–(Cu,Ag)–Al BMGs were measured under 200 g load by a Vickers diamond pyramidal microhardness tester (MH5, China) at room temperature. Cylindrical glassy rods (2 mm in diameter and 4 mm in height) of $Zr_{46}Cu_{46}Al_8$, $Zr_{46}(Cu_{4.5/5.5}Ag_{1/5.5})_{46}Al_8$ and $Zr_{45}(Cu_{4.5/5.5}Ag_{1/5.5})_{48}Al_7$ were used for compressive tests, which were performed using a universal testing machine (CMT5205 SANS, China) at a strain rate of 4×10^{-4} s^{-1} after calibration.

The acoustic longitudinal velocity (v_l) and shear velocity (v_s) of the $Zr_{46}Cu_{46}Al_8$, $Zr_{46}(Cu_{4.5/5.5}Ag_{1/5.5})_{46}Al_8$ and $Zr_{45}(Cu_{4.5/5.5}Ag_{1/5.5})_{48}Al_7$ BMGs were measured by a MATEC 6600 model ultrasonic system with a measuring sensitivity of 0.5 ns. The shape of sample was 5mm × 5mm × 1 mm. The carrying frequency of the ultrasonic is 5 MHz. Based on Archimedean principle, density (ρ) measurements of the $Zr_{46}Cu_{46}Al_8$ and $Zr_{46}(Cu_{4.5/5.5}Ag_{1/5.5})_{46}Al_8$ BMGs were performed with a Mettler Toledo XS105 microbalance having a sensitivity of 0.01 mg. The Young's modulus E, shear modulus G, bulk modulus K and Poisson's ratio v were derived from the acoustic velocities and the density data using the following equations [25,26]:

$$G = \rho V_s^2 \tag{6}$$

$$K = \rho\left(V_l^2 - \frac{4}{3}V_s^2\right) \tag{7}$$

$$v = (V_l^2 - 2V_s^2)/2(V_l^2 - V_s^2) \tag{8}$$

$$E = 2G(1 + v) \tag{9}$$

Corrosion behaviors of $Zr_{46}(Cu_{4.5/5.5}Ag_{1/5.5})_{46}Al_8$ BMGs were evaluated by electrochemical measurements. Specimens (3 mm in diameter and 6 mm in height) for corrosion test were closely sealed with epoxy resin and only leave an end-surface exposed for testing. Prior to the test, the testing surface of each specimen was mechanically polished to mirror finish, then degreased in acetone, washed in distilled water and further exposed to air for 24 h for good reproducibility. Electrolytes of 1 N H_2SO_4, 3 mass% NaCl, and 1 N HCl solutions open to air were used at room temperature (about 298 K). Polarization curves were measured with a potential sweep rate of 50 mV min^{-1} after open-circuit immersion for about 10 min when the open-circuit potential became almost steady. Electrochemical measurements were conducted in a three-electrode cell using a saturated calomel reference electrode (SCE) and platinum counter electrodes. For compression and corrosion experiments, at least three-time tests were performed for each composition to ensure reproducible results.

The thermal conductivity of $Zr_{46}(Cu_{4.5/5.5}Ag_{1/5.5})_{46}Al_8$ BMGs were measured on sheets with 10 mm × 10 mm × 1 mm sample size by NETZSCH LFA 457. Magnetic measurements for $Zr_{46}(Cu_{4.5/5.5}Ag_{1/5.5})_{46}Al_8$ BMG were performed using a vibrating sample magnetometer at room temperature (about 298 K).

3. Results

3.1. Glass-forming ability of $Zr_{100-x-y}(Cu_zAg_{1-z})_yAl_x$ alloys

Fig. 1a and 1b shows the selected DSC scanning of glassy alloys with variable Al and (Cu/Ag) contents, as well as the ratio of Cu/Ag at a heating rate of 20 K min^{-1}. Table 1 lists the critical sizes and thermal parameters of these glassy rods including glass transition temperature (T_g), onset crystallization temperature (T_x), melting temperature (T_m) and liquidus temperature (T_l), as well as supercooled liquid region, $\Delta T_x = T_x - T_g$, reduced glass transition temperature $T_g = T_g//T_l$ and γ value ($\gamma = T_x/(T_g + T_l)$) estimated by using a heating rate of 20 K min^{-1}. Other typical BMGs reported in the literature are also included for comparison [20,27,28]. It is found that with increasing the Al content from $x = 7$–9 at.%, T_g increases gradually from 703 to 710 K, while T_x decreases from 781 to 762 K, which result in the decrement of the supercooled liquid region. Al concentration significantly affects the glass-forming ability of the alloy system: with $x = 7$ and 8 at.%, wider composition range can form fully glassy 20 mm rods, while for $x = 9$ at.% it becomes much narrower. This can also be reflected by the two GFA indicators, T_{rg} and γ values. Fixing the Al content, we then examined the effect of (Cu,Ag) content on the thermal properties and GFA. It is found that the slight increment of (Cu,Ag) content (from 42 to 44 at.%) results in the distinct increment of T_g and reduction of T_l, leading to the increase of T_{rg} and γ values and enhancement of GFA. However, by further increasing the (Cu,Ag) content to 48 at.%, T_l quickly raises. Consequently, the T_{rg} and γ values come down and GFA deteriorates. The third factor, the

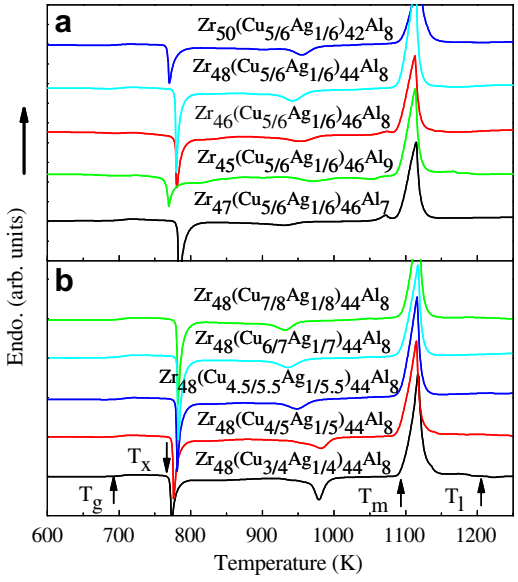

Fig. 1. DSC curves of glassy $Zr_{100-x-y}(Cu_zAg_{1-z})_yAl_x$ alloys at a constant heating rate 20 K min^{-1}: (a) variable Al and (Cu, Ag) contents; (b) variable Ag/Cu ratio.

Table 1
The critical sizes (d_c) and thermal parameters for $Zr_{100-x-y}(Cu_zAg_{1-z})_yAl_x$ ($x = 7$–9 at.%, $y = 42$–50 at.% and $z = 0.75$–0.875) alloys, together with other BMGs reported in Refs. [20,27,28] for comparison

Alloys	Critical size	Amorphous ingots (25 g)	T_g	T_x	T_m	T_l	ΔT_x	T_{rg}	γ
$Zr_{46}Cu_{46}Al_8$	5 mm	No	715	771	978	1163	56	0.615	0.411
$Zr_{47}(Cu_{4/5}Ag_{1/5})_{46}Al_7$	<20 mm	No	704	783	1055	1242	79	0.567	0.402
$Zr_{47}(Cu_{4.5/5.5}Ag_{1/5.5})_{46}Al_7$	<20 mm	Partial	702	782	1056	1123	80	0.625	0.428
$Zr_{47}(Cu_{5/6}Ag_{1/6})_{46}Al_7$	<20 mm	Partial	703	781	1060	1125	78	0.625	0.427
$Zr_{47}(Cu_{6/7}Ag_{1/7})_{46}Al_7$	20 mm	Partial	709	774	1057	1118	65	0.634	0.424
$Zr_{45}(Cu_{4/5}Ag_{1/5})_{48}Al_7$	20 mm	Partial	710	783	1062	1208	73	0.588	0.408
$Zr_{45}(Cu_{4.5/5.5}Ag_{1/5.5})_{48}Al_7$	>20 mm	Yes	711	785	1063	1154	74	0.616	0.421
$Zr_{45}(Cu_{5/6}Ag_{1/6})_{48}Al_7$	>20 mm	Yes	713	786	1061	1159	73	0.615	0.420
$Zr_{43}(Cu_{5/6}Ag_{1/6})_{50}Al_7$	20 mm	No	738	770	1075	1127	32	0.65	0.413
$Zr_{50}(Cu_{4/5}Ag_{1/5})_{42}Al_8$	20 mm	Partial	703	774	1089	1155	71	0.609	0.417
$Zr_{50}(Cu_{5/6}Ag_{1/6})_{42}Al_8$	<20 mm	Partial	701	764	1095	1138	63	0.616	0.415
$Zr_{48}(Cu_{3/4}Ag_{1/4})_{44}Al_8$	20 mm	Partial	706	770	1092	1218	64	0.580	0.400
$Zr_{48}(Cu_{4/5}Ag_{1/5})_{44}Al_8$	>20 mm	Yes	707	762	1090	1132	55	0.625	0.414
$Zr_{48}(Cu_{4.5/5.5}Ag_{1/5.5})_{44}Al_8$	>20 mm	Yes	706	777	1089	1129	71	0.625	0.423
$Zr_{48}(Cu_{5/6}Ag_{1/6})_{44}Al_8$	>20 mm	Yes	705	778	1090	1122	73	0.628	0.426
$Zr_{48}(Cu_{6/7}Ag_{1/7})_{44}Al_8$	>20 mm	Yes	706	778	1089	1127	72	0.626	0.424
$Zr_{48}(Cu_{7/8}Ag_{1/8})_{44}Al_8$	20 mm	Partial	707	779	1095	1127	72	0.627	0.425
$Zr_{46}(Cu_{4/5}Ag_{1/5})_{46}Al_8$	>20 mm	Yes	710	776	1091	1228	66	0.578	0.400
$Zr_{46}(Cu_{4.5/5.5}Ag_{1/5.5})_{46}Al_8$	>20 mm	Yes	703	775	1088	1126	72	0.624	0.424
$Zr_{46}(Cu_{4.5/5.5}Ag_{1/5.5})_{46}Al_8$ ingots	>20 mm	Yes	704	776	1089	1130	72	0.623	0.423
$Zr_{46}(Cu_{5/6}Ag_{1/6})_{46}Al_8$	>20 mm	Partial	710	778	1088	1120	68	0.634	0.425
$Zr_{53}(Cu_{5/6}Ag_{1/6})_{38}Al_9$	20 mm	Partial	711	767	1089	1129	56	0.63	0.417
$Zr_{51}(Cu_{4.5/5.5}Ag_{1/5.5})_{40}Al_9$	20 mm	Partial	703	758	1092	1144	55	0.615	0.410
$Zr_{49}(Cu_{5/6}Ag_{1/6})_{42}Al_9$	20 mm	Partial	708	767	1092	1242	59	0.57	0.393
$Cu_{43}Zr_{43}Al_7Ag_7$ [27]	8 mm	–	722	794	1125	–	72	–	–
$Zr_{41.2}Ti_{13.8}Cu_{12.5}Ni_{10}Be_{22.5}$ [28]	25 mm	–	623	672	932	996	49	0.67	0.415
$Pd_{40}Cu_{30}Ni_{10}P_{20}$ [28]	72 mm	–	575	670	804	840	95	0.72	0.473
$La_{62}Al_{14}Cu_{11.3}Ag_{2.7}Ni_5Co_5$ [20]	>20 mm	–	422	482	642	727	60	0.580	0.419
$La_{65}Al_{14}Cu_{9.2}Ag_{1.8}Ni_5Co_5$ [20]	35 mm	–	419	459	641	687	40	0.610	0.415

"Yes", "partial" and "no" are roughly defined by eyes for ingots having volume fractions of larger than about 80%, 30–80% and less than about 30% for the amorphous component, respectively.

ratio of Cu/Ag, is considered to refine the composition for higher GFA. Fig. 1b shows the influence of Cu/Ag ratio on thermal properties. All the curves in Fig. 1b exhibit typical endothermic characteristic before crystallization with glass transition around 706 K and large supercooled liquid region ΔT_x over 60 K. The almost single endothermic melting peak indicates that all these compositions, forming at least 20 mm BMGs, are near eutectic composition, which tallies with the criterion that eutectic compositions are generally more favorable for glass formation. It can be concluded that T_{rg} and γ two indicators can predict GFA in the Zr–(Cu,Ag)–Al alloy system with different Cu/Ag ratio. Element concentration plays crucial roles on the glass-forming ability of the Zr–(Cu,Ag)–Al alloy system. In the next step, meticulous scanning of compositions was carried out to get better glass formers.

Fig. 2a–2c shows the XRD patterns recorded from the cross-section of 20 mm diameter as-cast $Zr_{100-x-y}(Cu_zAg_{1-z})_yAl_x$ alloys with $x = 7$ at.% and $y = 46$–50 at.%; $x = 8$ at.% and $y = 42$–46 at.%; and $x = 9$ at.%, $y = 38$–42 at.% and $z = 0.75$–0.875. It is found that most of these alloys show broad diffraction humps, indicating their glassy nature. A wider composition range, which could be formed fully 20 mm amorphous rods, are listed in Table 1. To further ascertain the glassy nature, a

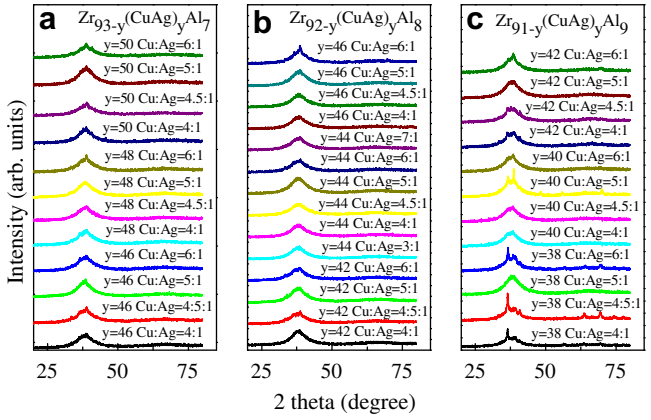

Fig. 2. XRD patterns for 20 mm $Zr_{100-x-y}(Cu_zAg_{1-z})_yAl_x$ quaternary alloys with different Al content x: (a) $x = 7$, (b) $x = 8$ and (c) $x = 9$, prepared by suction-casting into copper mold in a high-vacuum (2×10^{-5} torr) chamber under a purified argon atmosphere.

cross-section of 20 mm $Zr_{46}(Cu_{4.5/5.5}Ag_{1/5.5})_{46}Al_8$ alloy is selected to perform high-resolution X-ray diffraction scanning with 1×1 mm^2 beam size using synchrotron radiation source and a wavelength of 0.12398 Å. Fig. 3a illustrates a schematic map of scanned positions. From these about 20 HRXRD patterns presented in Fig. 3b and 3c, it is clear that all of the patterns consist of only a series of broad dif-

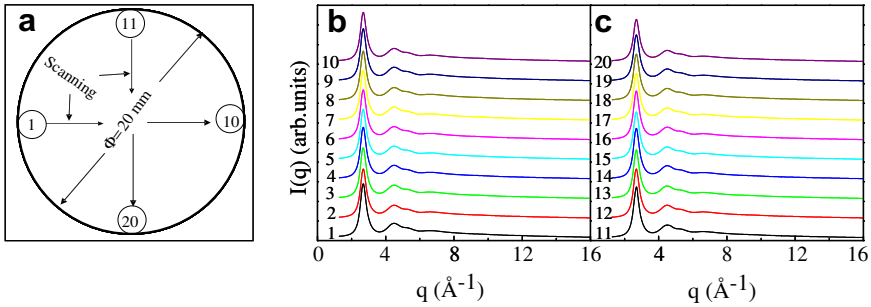

Fig. 3. (a) Illustration of scanning direction for recording 20 XRD patterns of 20 mm $Zr_{46}(Cu_{4.5/5.5}Ag_{1/5.5})_{46}Al_8$ BMG alloy; (b) and (c) are high-resolution X-ray diffraction patterns recorded using $1 \times 1\ mm^2$ beam size by synchrotron radiation at various positions (a) with a wavelength of 0.12398 Å.

fraction maxima without any detectable sharp Bragg peaks, confirming the fully amorphous structure of the 20 mm rod sample prepared here.

According to our experience, it is not unreasonable to expect the maximum critical size for glass formation in the pseudo ternary Zr–(Cu,Ag)–Al to be larger than 20 mm if we had a copper mold with larger diameter (>20 mm) using suction-casting in a high-vacuum (2×10^{-5} torr) chamber. Hence $Zr_{46}(Cu_{4.5/5.5}Ag_{1/5.5})_{46}Al_8$was selected to prepare rods with 30 mm in diameter by tilt-pouring the melt into copper mold with 30 mm cavity in a vacuum of 2×10^{-1} torr chamber. From the inset of Fig. 4, surface of the as-cast rod is smooth and exhibits metallic luster. However, due to extreme low-vacuum (2×10^{-1} torr), the XRD pattern of 30 mm rod presented in Fig. 4 shows a dominate amorphous component together with crystalline oxides ZrO (PDF 89-4768), Ag_2O, and Cu–Zr phases (CuZr, $CuZr_2$ and $Cu_{10}Zr_7$). Oxygen reacts with primary elements to form oxides, which might further induce crystallization to form crystalline phases, such as: CuZr, $Cu_{10}Zr_7$. Consequently, high oxygen content largely deteriorates GFA, which is consistent with data reported in other alloy systems [29,30]. We believe that the maximum critical size for forming BMGs in the Zr–(Cu,Ag)–Al alloy system is more than 20 mm if one uses a high-vacuum chamber for preparation, which is under construction.

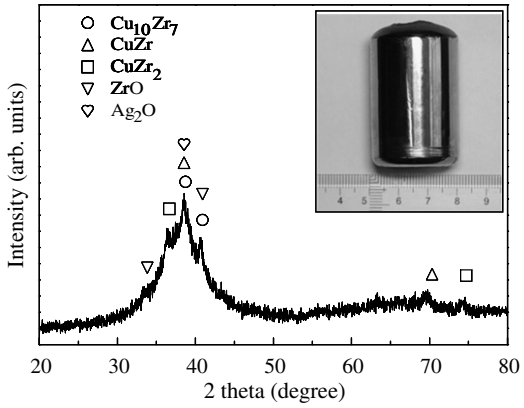

Fig. 4. XRD pattern for 30 mm $Zr_{46}(Cu_{4.5/5.5}Ag_{1/5.5})_{46}Al_8$ alloy prepared by tilt-pouring the melt into copper mold with 30 mm cavity in a vacuum of 2×10^{-1} torr chamber . The inset is the appearance of the as-cast 30 mm rod.

After cracking the arc-melted ingots, shining fracture surfaces were observed as presented in Fig. 5a. Hence, XRD and DSC were employed to examine their structure. Fig. 5b schematically shows the cross-section of a cracked ingot with about 28 mm in diameter and 30 g in weight. As the bottom part contacts with copper mold and its cooling rate is relatively lower; this part is crystalline. The samples taken for XRD and DSC measurements were illustrated in Fig. 5b. Fig. 5c shows DSC curves and XRD (inset of Fig. 5c) of the ingot and as-cast BMG sample with composition $Zr_{46}(Cu_{4.5/5.5}Ag_{1/5.5})_{46}Al_8$. Strikingly, XRD pattern

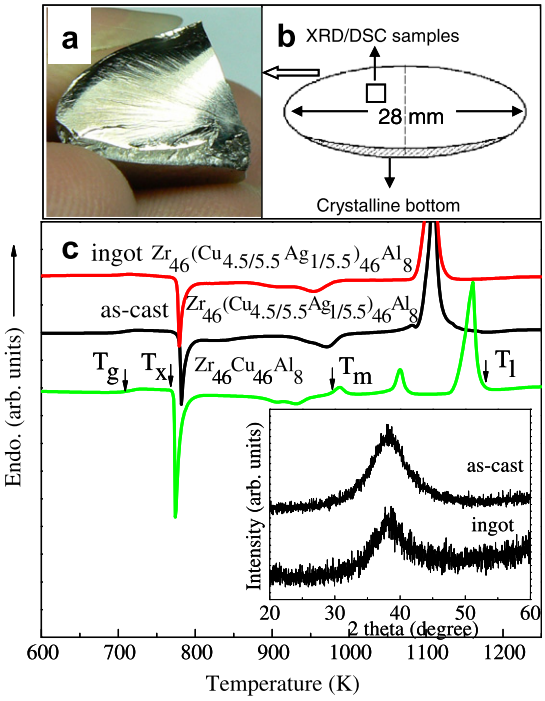

Fig. 5. (a) and (b) illustration of fractured surface of the arc-melted $Zr_{46}(Cu_{4.5/5.5}Ag_{1/5.5})_{46}Al_8$ ingot. (c) XRD patterns and DSC curves of the arc-melted $Zr_{46}(Cu_{4.5/5.5}Ag_{1/5.5})_{46}Al_8$ ingot and as-cast $Zr_{46}(Cu_{4.5/5.5}Ag_{1/5.5})_{46}Al_8$BMG sample, together with DSC curve of as-cast $Zr_{46}Cu_{46}Al_8$ BMG alloy.

and DSC curve of the ingot are nearly identical to those of the as-cast BMG. All the thermal parameters, including T_g, T_x, $\Delta T_x = T_x - T_g$, $T_{rg} = T_g/T_l$ and γ value ($\gamma = T_x/(T_g + T_l)$), are almost the same within the experimental uncertainty for both ingot and as-cast BMG. These results confirm amorphous structure in the ingot. Ingots with amorphous phase are found in a wide composition range, as listed in Table 1.

3.2. Properties of ZrCuAl and Zr–(Cu,Ag)–Al alloys

Mechanical properties and corrosion behaviors of the newly developed Zr–(Cu,Ag)–Al BMGs have been studied. Fig. 6 shows compressive stress–strain curves of the as-cast $Zr_{46}Cu_{46}Al_8$ and $Zr_{46}(Cu_{4.5/5.5}Ag_{1/5.5})_{46}Al_8$, $Zr_{45}(Cu_{4.5/5.5}Ag_{1/5.5})_{48}Al_7$ glassy rods at a strain rate of $4 \times 10^{-4}s^{-1}$. The compressive yield stress (σ_y), fracture stress (σ_f) and plastic strain (ε_p) were listed in Table 2. All the three stress–strain curves are characteristic of large elastic limits about 2% with different plastic strains. The mother alloy $Zr_{46}Cu_{46}Al_8$ exhibits $\sigma_y = 1673$ MPa and $\varepsilon_p = 3.6\%$. Ag addition remarkably improves its mechanical properties, leading to σ_y of 1800 MPa and 2100 MPa and significant plastic deformation for the two alloys: $Zr_{46}(Cu_{4.5/5.5}Ag_{1/5.5})_{46}Al_8$ and $Zr_{45}(Cu_{4.5/5.5}Ag_{1/5.5})_{48}Al_7$, respectively, especially for the latter alloy, ε_p reaches up to 28%. This alloy exhibits extraordinary compressive plasticity, high GFA (25 g amorphous ingot), high fracture strength, and cheap and non-toxic raw materials, which have never been reported previously in any other BMG alloy systems. According to three-dimensional atomic probe study [31], nanometer-scale (2–3 nm) Ag-rich phase separation was detected in a $Zr_{43}Cu_{43}Ag_7Al_7$BMG, which might occur in the present alloy too because of similar compositions. Thus, the phase separation could be a conceivable factor in the present alloy to the extraordinary compressive plasticity, in which nanometer-sized heterogeneities in the sample could act both as initiation sites for shear bands and as barriers to shear band propagation, resulting in an increase of compressive plasticity. The understanding of the mechanism for such high compressive plasticity for the present alloy is in progress.

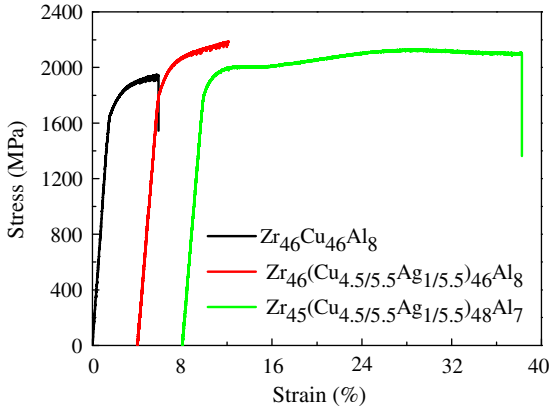

Fig. 6. Compressive stress–strain curves of as-cast $Zr_{46}Cu_{46}Al_8$, $Zr_{46}(Cu_{4.5/5.5}Ag_{1/5.5})_{46}Al_8$ and $Zr_{45}(Cu_{4.5/5.5}Ag_{1/5.5})_{48}Al_7$ glassy rods with 2 mm in diameter and 4 mm in length at a strain rate of 4×10^{-4}/s at room temperature.

Ultrasonic measurements were also carried out to determine the elastic constants of these Zr–(Cu,Ag)–Al BMGs. Their values are listed in Table 2. For comparison, the values of other ZrCu-based BMGs, such as $Zr_{50}Cu_{50}$, $Zr_{47.5}Cu_{47.5}Al_5$ and $Cu_{43}Zr_{43}Al_7Ag_7$, were also included [27,32]. In addition, hardness (V_c) and thermal conductivity (λ) are also measured for the newly developed $Zr_{46}(Cu_{4.5/5.5}Ag_{1/5.5})_{46}Al_8$ alloy, to be $V_c = 533 \pm 3$ and $\lambda = 5.3$ W m^{-1} K^{-1}, respectively. The alloy is paramagnetic at ambient temperature.

The corrosion behavior of $Zr_{46}(Cu_{4.5/5.5}Ag_{1/5.5})_{46}Al_8$ BMG in three types of solutions were tested. Fig. 7 shows the potentiodynamic polarization curves of $Zr_{46}(Cu_{4.5/5.5}Ag_{1/5.5})_{46}Al_8$ BMGs in 1N H_2SO_4, 3mass% NaCl, and 1N HCl solutions open to air at 298 K, respectively. In 1N H_2SO_4, the $Zr_{46}(Cu_{4.5/5.5}Ag_{1/5.5})_{46}Al_8$ alloy is passivated with a corrosion potential of about −0.5 V and a relatively low passive current density of about 2.8×10^{-4} A cm^{-2}, indicating that protective surface film was formed immediately by anodic polarization. The polarization curve of $Zr_{46}(Cu_{4.5/5.5}Ag_{1/5.5})_{46}Al_8$ alloy in 1N H_2SO_4 shows wider passive region (−0.3−1.5 V) before trans-passive corrosion occurred. The slow change in the corrosion density with anodic potential at above 2 V implies a general corrosion. In 3mass% NaCl and 1N HCl solutions, the $Zr_{46}(Cu_{4.5/5.5}Ag_{1/5.5})_{46}Al_8$ alloys dissolve actively and their

Table 2
Mechanical properties obtained by compression test and elastic constants including elastic modulus (E), bulk modulus (K), shear modulus (G) and Poisson's ratio (ν), obtained by ultrasonic measurements for newly developed Zr–(Cu,Ag)–Al bulk metallic glasses together with those for other BMGs in Refs. [27,32]

Glasses	ρ (g cm^{-3})	E (GPa)	G (GPa)	K (GPa)	ν	σ_y (MPa)	σ_f (MPa)	ε_p (%)
$Zr_{46}Cu_{46}Al_8$	7.021	96.4	35.2	121.6	0.368	1673	1931	3.6
$Zr_{46}(Cu_{4.5/5.5}Ag_{1/5.5})_{46}Al_8$	7.177	92.4	33.8	115.5	0.367	1822	2163	6.0
$Zr_{45}(Cu_{4.5/5.5}Ag_{1/5.5})_{48}Al_7$	7.322	93.5	34.2	119	0.369	1839	2105	28.1
$Zr_{50}Cu_{50}$ [27,32]	–	84.0	31.3	101.2	0.35	1745	1781	3.9–4.9
$Zr_{47.5}Cu_{47.5}Al_5$ [27,32]	–	90.1	33.0	113.7	0.365	1700	1800	4.0–5.0
$Zr_{42}Cu_{42}Al_7Y_5$ [27,32]	–	84.6	31	104.1	0.364	–	–	–
$Zr_{43}Cu_{43}Al_7Ag_7$ [32]	–	–	–	–	–	1771	1745	4.9–7.0

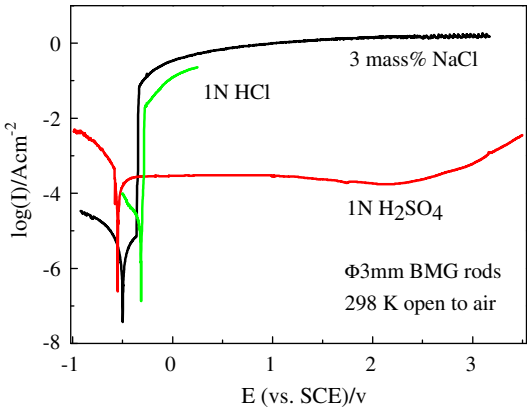

Fig. 7. Potentiodynamic polarization curves of as-cast $Zr_{46}(Cu_{4.5/5.5}Ag_{1/5.5})_{46}Al_8$ alloys in 1 N H_2SO_4, 3 mass% NaCl, and 1 N HCl solutions open to air at room temperature (at 298 K).

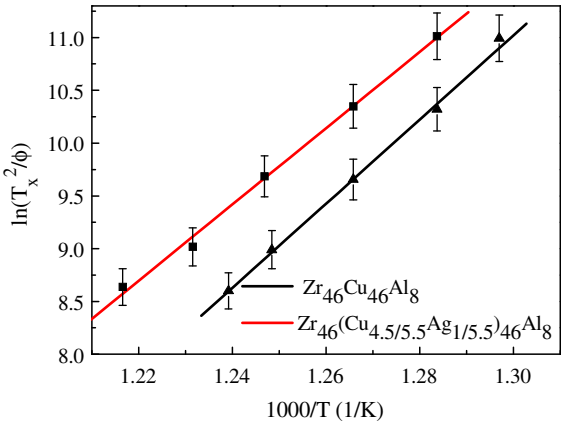

Fig. 8. Kissinger plots of the onset crystallization temperatures T_x at different heating rates for $Zr_{46}Cu_{46}Al_8$ and $Zr_{46}(Cu_{4.5/5.5}Ag_{1/5.5})_{46}Al_8$ glassy alloys.

anodic current densities increase quickly by anodic polarization. Pit nucleation appears at potentials of about −0.5 V and −0.3 V in 3mass% NaCl and 1N HCl solutions, respectively. Similar results were also reported in $Zr_{52.5}Cu_{17.9}Ni_{14.6}Al_{10}Ti_5$ and $Cu_{60}Hf_{25}Ti_{15}$ BMGs [33,34]. It can be concluded that the newly developed $Zr_{46}(Cu_{4.5/5.5}Ag_{1/5.5})_{46}Al_8$ BMG exhibits excellent corrosion resistance in H_2SO_4 solution, rather poor in solutions containing Cl^{-1} ions. To improve the latter, more effort is needed.

Compared with crystalline materials, BMGs are metastable and devitrify upon heating. In view that crystallization kinetics could redound to the understanding of thermal stability of BMGs, DSC measurements with different heating rates ($\phi = 10$–120 K min^{-1}) were performed for the $Zr_{46}(Cu_{4.5/5.5}Ag_{1/5.5})_{46}Al_8$ BMG together with $Zr_{46}Cu_{46}Al_8$ BMG for comparison. It is found that for both BMGs the glass transition temperature and crystallization temperatures shift to higher values with increasing heating rates. Fig. 8 presents Kissinger's plots of the onset crystallization temperatures T_x at different heating rates based in Eq. (10) [35]:

$$\ln\frac{T^2}{\phi} = \frac{E_a}{RT} + \text{const} \tag{10}$$

where R is the gas constant, and E_a is the activation energy for crystallization. The activation energies of crystallization E_a for $Zr_{46}Cu_{46}Al_8$ and $Zr_{46}(Cu_{4.5/5.5}Ag_{1/5.5})_{46}Al_8$ alloys are evaluated to be 3.30 eV and 3.01 eV, respectively, listed in Table 4. Ag addition leads to the slight decrease of E_a value. However, compared with other BMGs [10,26], the newly developed Zr–(Cu,Ag)–Al BMG alloys show relatively higher E_a values. Generally, the larger the E_a value, the higher additional energy needed for atomic diffusion from glassy state to crystalline one.

4. Discussion

Glass-forming ability is a competition between cooling rate and crystallization kinetics, which is closely related to structural, thermodynamic and kinetic characteristic. From a structural point of view, the significant difference in the atomic sizes and negative heats of mixing could lead to an increase of random packing density in the supercooled liquid and hence increase the difficulty for atomic diffusion. Kinetically, the viscosity is an important parameter for structural rearrangement of atoms in undercooled liquid to the growth of a crystal nucleus. Thermodynamically, lower $\Delta G_{l-s}(T)$ (Gibbs free energy difference of the undercooled liquid with respect to the crystal) is expected to stabilize the undercooled melt against crystallization. Attempts have been made to probe the glass-forming mechanism from all these three aspects. However, for different alloy systems, factors determining the glass formation may change from one to another [4,10,36–44]. To understand the underlying physics of the beneficial effects of Ag addition in the present alloy system, a systematical study in terms of the structural, fragility index, and thermodynamic factors was carried out for $Zr_{46}(Cu_{4.5/5.5}Ag_{1/5.5})_{46}Al_8$ BMG together with $Zr_{46}Cu_{46}Al_8$ BMG for comparison.

Structural aspects including atomic sizes and negative heats of mixing were considered to probe the origin of high GFA in the present Ni-free Zr–(Cu,Ag)–Al system. Atomic radii of elements are Zr 0.160 nm, Al 0.143 nm, Cu 0.128 nm and Ag 0.144 nm [45]. The ratios of atomic radii are estimated to be $R_{Zr/Ag} = 1.111$, $R_{Al/Cu} = 1.117$, $R_{Zr/Cu} = 1.250$ and $R_{Zr/Al} = 1.119$. Heat-of-mixing values between elements are: Zr–Cu: −23 kJ mol^{-1}, Zr–Ag: −20 kJ mol^{-1}, Zr–Al: −44 kJ mol^{-1}, Cu–Al: −1 kJ mol^{-1} and Cu–Ag: 2 kJ mol^{-1} [46]. The large negative heat-of-mixing values of main components and intermediate atomic mismatches basically satisfy the Inoue's empirical rules [4]: atomic size mismatch (>12%) and large negative heating of mixing, which were proposed to enhance local random packing density and GFA.

Fig. 9 shows the structural factors, $S(q)$, and pair correlation function, $g(r)$, for $Zr_{46}Cu_{46}Al_8$ and $Zr_{46}(Cu_{4.5/5.5}Ag_{1/5.5})_{46}Al_8$ BMG alloys. Peak positions and

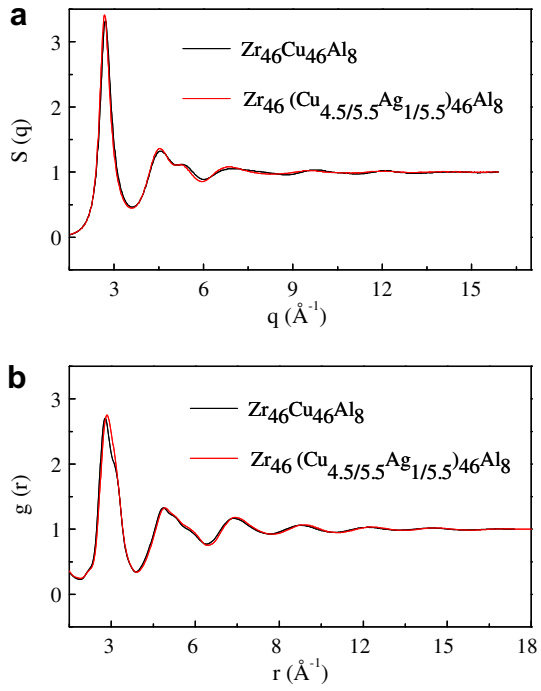

Fig. 9. (a) Structure factors, $S(q)$, and (b) pair correlation function, $g(r)$, for the glassy $Zr_{46}Cu_{46}Al_8$ and $Zr_{46}(Cu_{4.5/5.5}Ag_{1/5.5})_{46}Al_8$ alloys at room temperature recorded by using synchrotron radiation HRXRD with a wavelength of 0.12398 Å.

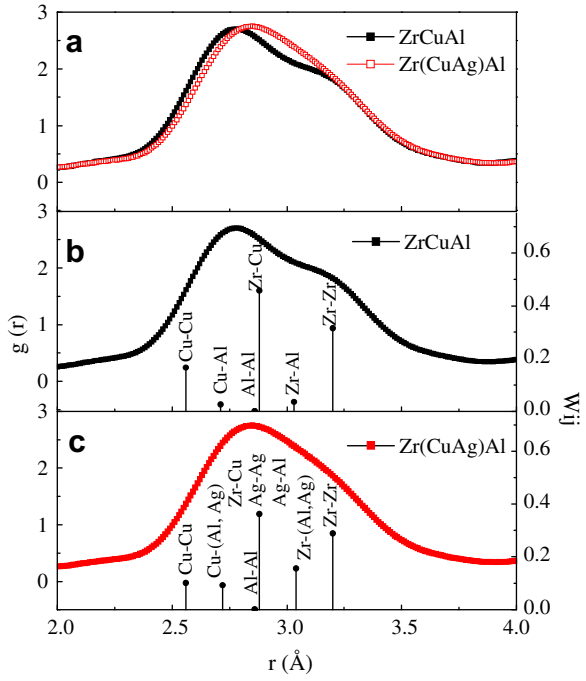

Fig. 10. The first peaks of pair correlation function, $g(r)$, for the $Zr_{46}Cu_{46}Al_8$ and $Zr_{46}(Cu_{4.5/5.5}Ag_{1/5.5})_{46}Al_8$ glassy alloys. (a) Enlargement of the first peaks of $g(r)$. (b) the first peak of $g(r)$ for $Zr_{46}Cu_{46}Al_8$ alloy, (c) the first peak of $g(r)$ for $Zr_{46}(Cu_{4.5/5.5}Ag_{1/5.5})_{46}Al_8$ alloy. The bars indicate the interatomic distances from hard sphere model. The height of the bars corresponds to partial structure factor weight values.

profiles in the $S(q)$ and $g(r)$ curves of $Zr_{46}Cu_{46}Al_8$ and $Zr_{46}(Cu_{4.5/5.5}Ag_{1/5.5})_{46}Al_8$ are similar. Considering peaks in the nearest atomic pairs, revealing information about the short-range order, we enlarged curves of the first peaks of pair correlation function, $g(r)$ in Fig. 10a. Using the hard sphere model the difference in the first $g(r)$ peaks will be discussed. Interatomic distances and concentration-weighted partial radial distribution values for $Zr_{46}Cu_{46}Al_8$ and $Zr_{46}(Cu_{4.5/5.5}Ag_{1/5.5})_{46}Al_8$ alloys are indicated in Fig. 9b and 9c and also listed in Table 3. Zr–Zr, Zr–Cu and Cu–Cu atomic pairs dominate the first peak. In the $Zr_{46}(Cu_{4.5/5.5}Ag_{1/5.5})_{46}Al_8$ alloy, in which the atomic radius of Ag almost equals that of Al, the primary bonds become complex. Since the concentration-weighted value for Zr–Cu atomic pair decreases and those for Zr–Ag, Cu–Ag, Ag–Ag and Ag–Al atomic pairs increase due to Ag addition, the first peak of $g(r)$ slightly shift to high r value. More bonds exist in the quaternary system and the pair radial distribution, thus, becomes uniform, especially at about $r = 2.72$ Å and $r = 3.03$ Å. The shoulder, appearing in the $g(r)$ curve of $Zr_{46}Cu_{46}Al_8$, becomes less prominent in $Zr_{46}(Cu_{4.5/5.5}Ag_{1/5.5})_{46}Al_8$ alloy. Coordination number, N_c, a key parameter to access the atomic packing density, could be deduced by integrating the radial distribution function over the range of the first peak. The coordination number was found to be slightly larger for the quaternary $Zr_{46}(Cu_{4.5/5.5}Ag_{1/5.5})_{46}Al_8$ BMG alloy than that for the ternary $Zr_{46}Cu_{46}Al_8$ BMG alloy. The structural results and density values obtained in the present work indicate that the quaternary $Zr_{46}(Cu_{4.5/5.5}Ag_{1/5.5})_{46}Al_8$ BMG alloy has a slight denser local random packing than that for the ternary $Zr_{46}Cu_{46}Al_8$ BMG alloy.

The kinetic and thermodynamic aspects are of great importance in understanding the dynamic nature of glass transition, structural rearrangement and GFA, which reflects the competition between cooling rate and crystallization kinetics [39–43]. According to the classical nucleation theory, the steady-state crystal nucleation

Table 3
Interatomic distances estimated from the hard sphere model and concentration-weighted partial radial distribution for (A) $Cu_{46}Zr_{46}Al_8$, (B) $Zr_{46}(Cu_{4.5/5.5}Ag_{1/5.5})_{46}Al_8$ alloys

Bond type	Cu–Cu	Cu–Ag	Cu–Zr	Cu–Al	Ag–Ag	Ag–Zr	Ag–Al	Zr–Zr	Zr–Al	Al–Al
D (Å)	2.56	2.72	2.88	2.71	2.88	3.04	2.87	3.2	3.03	2.86
W_{ij} (A)	0.166	–	0.457	0.026	–	–	–	0.315	0.036	0.001
W_{ij} (B)	0.101	0.073	0.342	0.019	0.013	0.123	0.007	0.288	0.033	0.001

rate per unit volume, I_{ss}, can reflect the interplay between the kinetics and thermodynamics, which is expressed as:

$$I_{ss} = \frac{A}{\eta(T)} \exp\left(-\frac{16\pi\sigma^3}{2k_B[\Delta G_{l-s}(T)]^2}\right) \quad (11)$$

where A is a constant, $\eta(T)$ the temperature dependence of viscosity of the supercooled liquid, σ the interfacial energy between the liquid and the crystal, and $\Delta G_{l-s}(T)$ the Gibbs free energy difference between the supercooled liquid state and the crystalline state. High GFA expects a higher viscosity around melting temperature and a lower driving force $\Delta G_{l-s}(T)$. The viscosity at melting point is generally correlated with the liquid fragility, which is defined as [38]:

$$m = \left.\frac{d\log(\tau)}{d(T_g/T)}\right|_{T=T_g} \quad (12)$$

where τ is the average relaxation time, T the temperature. The well-known fragility parameter could be used to classify glass-forming liquid into strong and fragile [38]. Generally, a strong liquid usually has a higher viscosity at the melting point than a fragile one. The fragility parameter m can be calculated using Eq. (13) [47]:

$$m = \frac{DT_0T_g}{(T_g - T_0)^2 \ln 10} \quad (13)$$

where D is the strength parameter in the Vogel–Fulcher–Tammann (VFT) equation, and T_0 describes the onset of the glass transition in the limit of ϕ close to 0. These parameters can be obtained by fitting the VFT equation from the heating rate dependence of the glass transition temperature:

$$\ln\phi = \ln B - \frac{DT_0}{T_g - T_0} \quad (14)$$

where B is a parameter of time scale in the glass-forming system.

Fig. 11 gives the dependence of T_g on heating rate fitted by VFT equation. The fitted parameters and fragility index m are given in Table 4. The m values are $m = 43$ for $Zr_{46}Cu_{46}Al_8$ and $m = 49$ for $Zr_{46}(Cu_{4.5/5.5}Ag_{1/5.5})_{46}Al_8$, which are similar to the values reported for $Cu_{50}Zr_{50}$ ($m = 46$) and $Zr_{42}Cu_{42}Al_7Y_5$ ($m = 40$) BMGs [32]. These values can be classified to the intermediate fragile liquids and are larger than the rare earth alloys [10,26]. As the viscosity η also follows the VFT equation:

$$\eta = \eta_0 \exp\left(\frac{DT_0}{T_g - T_0}\right) \quad (15)$$

where η_0 the infinite temperature viscosity, one can get the viscosity at the melting temperature based on the fitted parameters D and T_0. The values obtained for $Zr_{46}Cu_{46}Al_8$ and $Zr_{46}(Cu_{4.5/5.5}Ag_{1/5.5})_{46}Al_8$ are 0.137 and 0.117 Pa s, which are comparable with the values listed in Ref. [32]. Ag addition slightly decreases the viscosity. Hence, kinetic aspect fails to explain the enhancement of GFA in the Zr–(Cu,Ag)–Al system.

Thermodynamically, nucleation does not occur unless the driving force exceeds the activation barrier for nucleation:

$$\Delta G^* = \frac{16\pi\sigma^3}{3\Delta G_{l-s}(T)^2} \quad (16)$$

Table 4
The parameters obtained from the heating rate dependence of the onset of crystallization temperature and glass transition temperature, including the activation energy E_a, T_0, strength parameter D, $\ln B$, fragility index m and viscosity η at T_m

Alloys	E_a (eV)	T_0 (K)	D	$\ln B$	m	η at T_m (Pa s)
A	3.3	588	3.88	20.75	43	0.137
B	3.0	578	4.77	24.07	49	0.117

$Zr_{46}Cu_{46}Al_8$ and $Zr_{46}(Cu_{4.5/5.5}Ag_{1/5.5})_{46}Al_8$ alloys are labeled as A and B in Table 1, respectively.

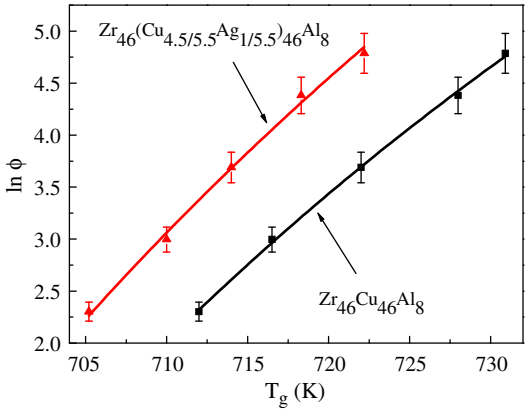

Fig. 11. The dependence of T_g on heating rate fitted by VFT equation for $Zr_{46}Cu_{46}Al_8$ and $Zr_{46}(Cu_{4.5/5.5}Ag_{1/5.5})_{46}Al_8$ glassy alloys.

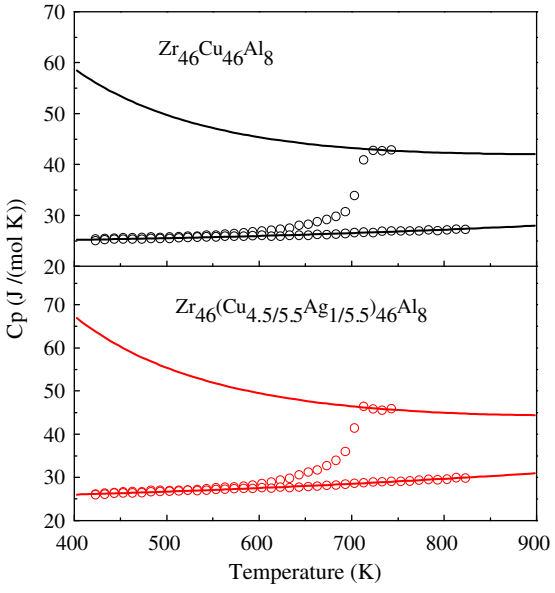

Fig. 12. Specific heat capacities (C_p) of (a) $Zr_{46}Cu_{46}Al_8$ and (b) $Zr_{46}(Cu_{4.5/5.5}Ag_{1/5.5})_{46}Al_8$ alloys measured in the crystalline, supercooled liquid and amorphous state.

Table 5
Fitting parameters from the heat capacity data, using to fit the crystalline state heat capacity data and to fit the liquid heat capacity data, together with the melting point T_m, the heat of fusion ΔH_m, the entropy of fusion $\Delta S_m = \Delta H_m/T_m$ and Kauzmann temperature T_K for the $Zr_{46}Cu_{46}Al_8$ and $Zr_{46}(Cu_{4.5/5.5}Ag_{1/5.5})_{46}Al_8$ alloys, which are labeled as A and B in Table 5, respectively

Alloys	a (J mol^{-1} K^{-2})	b (J mol^{-1} K^{-3})	c (J mol^{-1} K^{-2})	d (J mol^{-1} K^{-2})	T_m (K)	ΔH_m (kJ mol^{-1})	ΔS_m (J mol^{-1} K^{-1})	T_k (K)
A	−0.00166	5.59×10^{-6}	0.01268	4.6084×10^{6}	979	8.035	8.208	596
B	−0.000504	8.0089×10^{-6}	0.01348	5.931×10^{6}	1063	7.104	6.683	671

Lower $\Delta G_{l-s}(T)$ and higher σ result in the greater stability of the melt from crystallization. For the reason that it is hard for us to get the σ value, here only the ΔG_{l-s} will be evaluated based on the specific heat capacities. The high thermal stability allows us to get the heat capacity of these alloys in a wide range of undercooled liquid. Fig. 12 shows the specific heat capacities of $Zr_{46}Cu_{46}Al_8$ and $Zr_{46}(Cu_{4.5/5.5}Ag_{1/5.5})_{46}Al_8$ alloys, which were measured in the crystalline, supercooled liquid and amorphous state. The heat capacity of the glassy phases is similar to that of the crystalline ones before glass transition temperature, which is consistent with data reported in other alloys. However, with the increase of temperature, the glassy phases begin to relax and the heat capacities simultaneously rise. These specific heat capacity data of the undercooled liquid and the crystal are fitted using the following relationships [24,41]:

$$C_p^s = 3R + aT + bT^2 \tag{17}$$

$$C_p^l = 3R + cT + dT^{-2} \tag{18}$$

where $R = 8.3142$ J g atom^{-1}K^{-1} and a, b, c, and d are fitting constants. Table 5 lists the fitting results together with heat of fusion ΔH_m, the entropy of fusion $\Delta S_m = \Delta H_m/T_m$ at the melting point T_m for $Zr_{46}Cu_{46}Al_8$ and $Zr_{46}(Cu_{4.5/5.5}Ag_{1/5.5})_{46}Al_8$ alloys obtained in this work. Based on the above experimental data, the thermodynamic parameters, including enthalpy change $\Delta H_{l-s}(T)$ and entropy change $\Delta S_{l-s}(T)$ of the undercooled liquid with respect to the crystal can be calculated according to the following equations:

$$\Delta H_{l-s}(T) = \Delta H_m - \int_T^{T_m} [C_p^l(T) - C_p^s(T)]\,dT \tag{19}$$

$$\Delta S_{l-s}(T) = \Delta S_m - \int_T^{T_m} \frac{C_p^l(T) - C_p^s(T)}{T}\,dT \tag{20}$$

The results are plotted in Fig. 13. For both alloys, it is found that that the enthalpy of supercooled liquid decreases more slowly than the entropy, which leads to the entropy crisis. The Kauzmann temperature T_K is a theoretical temperature, at which $\Delta S_{l-s} = 0$ or the entropy of the liquid equals to the entropy of the crystalline, to be 596 K for $Zr_{46}Cu_{46}Al_8$ and 671 K for $Zr_{46}(Cu_{4.5/5.5}Ag_{1/5.5})_{46}Al_8$ alloy.

The Gibbs free energy difference $\Delta G_{l-s}(T)$ can be calculated as

$$\Delta G_{l-s}(T) = \Delta H_{l-s} - \Delta S_{l-s}T \tag{21}$$

Fig. 14 shows the Gibbs free energy differences for $Zr_{46}Cu_{46}Al_8$ and $Zr_{46}(Cu_{4.5/5.5}Ag_{1/5.5})_{46}Al_8$ BMG alloys together with data reported for other alloys as a function of temperature normalized to the melting point of the corresponding alloy. The ΔG_{l-s} value at T_k for $Zr_{46}(Cu_{4.5/5.5}Ag_{1/5.5})_{46}Al_8$ is 1.5 kJ mol^{-1} while for $Zr_{46}Cu_{46}Al_8$ alloy is about 1.8 kJ mol^{-1}. For comparison, the values of other bulk metallic glass formers were also listed here [10,41,43,44]: $Zr_{62}Ni_{38}$ 3.65 kJ mol^{-1}; $Cu_{47}Ti_{34}Zr_{11}Ni_8$ 3.5 kJ mol^{-1}; $Mg_{65}Cu_{25}Y_{10}$ 3.3 kJ mol^{-1}; $Pt_{57.3}Cu_{14.6}Ni_{5.3}P_{22.8}$ 3.2 kJ mol^{-1}; $Zr_{48.75}Ti_{8.25}Cu_{7.5}Ni_{10}Be_{27.5}$ 2.5 kJ mol^{-1}; $Zr_{41.2}Ti_{13.8}Cu_{12.5}Ni_{10}Be_{22.5}$ 2.2 kJ mol^{-1}; $Zr_{52.5}$

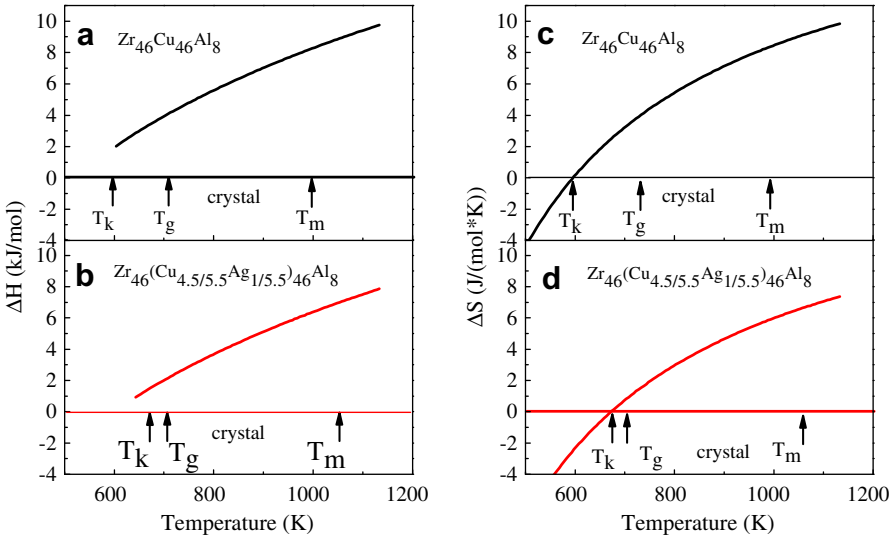

Fig. 13. Enthalpy change $\Delta H_{l-s}(T)$ and entropy change $\Delta S_{l-s}(T)$ of the undercooled liquid with respect to the crystal of (a,c) $Zr_{46}Cu_{46}Al_8$, and (b,d) $Zr_{46}(Cu_{4.5/5.5}Ag_{1/5.5})_{46}Al_8$ alloys, respectively. Kauzmann temperatures T_K for the two alloys are indicated by arrows in the plots.

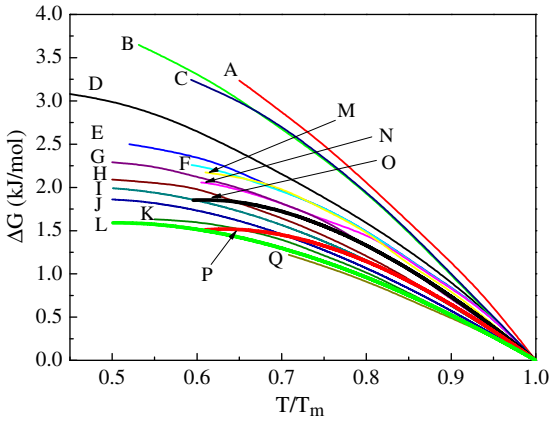

Fig. 14. Gibbs free energy difference $\Delta G_{l-s}(T)$ of the undercooled liquid with respect to the crystal of (A) $Pt_{57.3}Cu_{14.6}Ni_{5.3}P_{22.8}$ [44]; (B) $Zr_{62}Ni_{38}$ [44]; (C) $Cu_{47}Ti_{34}Zr_{11}Ni_8$ [44]; (D) $Mg_{65}Cu_{25}Y_{10}$ [44]; (E) $Zr_{48.75}Ti_{8.25}Cu_{7.5}Ni_{10}Be_{27.5}$ [44]; (F) $Zr_{41.2}Ti_{13.8}Cu_{12.5}Ni_{10}Be_{22.5}$ [44]; (G) $La_{55}Al_{25}Ni_{20}$ [41]; (H) $La_{55}Al_{25}Cu_{10}Ni_{10}$ [41]; (I) $La_{62}Al_{14}Cu_{24}$ [10]; (J) $La_{62}Al_{14}Cu_{20}Ag_4$ [10]; (K) $La_{55}Al_{25}Cu_{10}Ni_5Co_5$ [41]; (L) $La_{62}Al_{14}Cu_{11.3}Ag_{2.7}Ni_5Co_5$ [10]; (M) $Zr_{52.5}Cu_{17.9}Ni_{14.6}Al_{10}Ti_5$ [44]; (N) $Zr_{57}Cu_{15.4}Ni_{12.6}Al_{10}Nb_5$ [44], (O) $Zr_{46}Cu_{46}Al_8$; (P) $Zr_{46}(Cu_{4.5/5.5}Ag_{1/5.5})_{46}Al_8$; (Q) $Pd_{40}Ni_{10}Cu_{30}P_{20}$ [44].

$Cu_{17.9}Ni_{14.6}$ $Al_{10}Ti_5$ 2.2 kJ mol^{-1}; $Zr_{57}Cu_{15.4}Ni_{12.6}Al_{10}Nb_5$ 2.1 kJ mol^{-1}; $La_{55}Al_{25}Ni_{20}$ 2.29 kJ mol^{-1}; $La_{55}Al_{25}Cu_{10}Ni_{10}$ 2.1 kJ mol^{-1}; $La_{62}Al_{14}Cu_{24}$ 2.0 kJ mol^{-1}; $La_{62}Al_{14}Cu_{20}Ag_4$ 1.82 kJ mol^{-1}, $La_{55}Al_{25}Cu_{10}Ni_5Co_5$ 1.63 kJ mol^{-1}; $La_{62}Al_{14}Cu_{11.3}Ag_{2.7}Ni_5Co_5$ 1.5 kJ mol^{-1}; $Pd_{40}Ni_{10}Cu_{30}P_{20}$ 1.22 kJ mol^{-1}. Both $Zr_{46}Cu_{46}Al_8$ and $Zr_{46}(Cu_{4.5/5.5}Ag_{1/5.5})_{46}Al_8$ alloys show low Gibbs free energy difference, which are even lower than that of $Zr_{41.2}Ti_{13.8}Cu_{12.5}Ni_{10}Be_{22.5}$. Ag addition slightly decreases the value of the Gibbs free energy difference of $Zr_{46}(Cu_{4.5/5.5}Ag_{1/5.5})_{46}Al_8$ BMG alloy to the value close to $Pd_{40}Ni_{10}Cu_{30}P_{20}$ (critical size for BMG is 72 mm [4]) and $La_{62}Al_{14}Cu_{11.3}Ag_{2.7}Ni_5Co_5$ (critical size for BMG is 35 mm [10]). The relative lower ΔG_{l-s} value implies smaller driving force for crystallization, turning out to be one crucial factor in interpreting high GFA of $Zr_{46}(Cu_{4.5/5.5}g_{1/5.5})_{46}Al_8$ BMG alloy.

5. Conclusions

Meticulous scanning of the Zr–(Cu,Ag)–Al composition range was pursued to obtain better glass formers. Systematical investigation for the mechanism of their high GFA was carried out. Results obtained in the present work can be summarized as follows:

(1) Fully glassy alloys with at least 20 mm in diameter can be fabricated in a wide Zr–(Cu,Ag)–Al composition range using copper mold suction method. About 25 g amorphous metallic ingots can be detected in a wide Zr–(Cu,Ag)–Al composition range using conventional arc-melting machine.

(2) Two GFA indicators, T_{rg} and γ, can correlate with GFA of the studied Zr–(Cu,Ag)–Al alloy system.

(3) Various properties of a selected $Zr_{46}(Cu_{4.5/5.5}Ag_{1/5.5})_{46}Al_8$ BMG were characterized. The alloy shows good thermal and mechanical properties: glass transition temperature $T_g = 703$ K, relatively wide supercooled liquid region $\Delta T_x = 72$ K, high activation energy for crystallization $E_a = 3.0$ eV, fragility parameter $m = 49$, yield strength $\sigma_y = 1822$ MPa, fracture strength $\sigma_f = 2163$ GPa, Vicker's hardness $V_c = 533 \pm 3$, density $\rho = 7.177$ g cm^{-3}, Young's modulus $E = 92$ GPa, shear modulus $G = 33.8$ GPa, and Poisson ratio $\upsilon = 0.367$. It also exhibits high corrosion resistance in H_2SO_4 solution.

(4) The combination of high glass-forming ability (critical sizes for BMG more than 20 mm), relatively wide supercooled liquid region $\Delta T_x = 72$ K, excellent mechanical properties (up to 2100 MPa fracture strength and about 28% compressive plasticity), high corrosion resistance (in H_2SO_4 solution), with cheap and environmentally friendly raw materials enables to make the newly developed Zr–(Cu,Ag)–Al BMG alloys as promising engineering materials.

(5) The effect of Ag addition on glass-forming ability of the quaternary alloy has been systematically investigated from the structural, thermodynamic and kinetic points of view. The origin of high glass-forming ability in the studied system is attributed to denser local atomic packing and the smaller difference in Gibbs free energy between amorphous and crystalline phases of Zr–(Cu,Ag)–Al BMGs (for $Zr_{46}(Cu_{4.5/5.5}Ag_{1/5.5})_{46}Al_8$, $\Delta G_{l-s} = 1.5$ kJ mol^{-1}).

Acknowledgements

The authors would like to thank the HASYLAB staff at Hamburg, Germany, for the assistance during the measurements at BW5. Financial support from the National Natural Science Foundation of China (Grants Nos. 50341032, 50425102, 50601021, 5070138 and 60776014), Zhejiang University – Helmholtz cooperation fund, the Ministry of Education of China (Program for Changjiang Scholars and Ph.D. research fund), Zhejiang University and the EU-project (Ductile BMG Composites MRTN-CT-2003-504692) is gratefully acknowledged.

References

[1] Klement W, Willens RH, Duwez P. Nature 1960;187:869.
[2] Greer AL. Science 1995;267:1947.
[3] Johnson WL. MRS Bull 1999;24:42.
[4] Inoue A. Acta Mater 2000;48:279.
[5] Greer AL, Ma E. MRS Bull 2007;32:611.
[6] Nishiyama N, Inoue A. Mater Trans JIM 1996;37:1531.
[7] Peker A, Johnson WL. Appl Phys Lett 1993;63:2342.
[8] Guo F, Poon SJ, Shiflet GJ. Appl Phys Lett 2003;83:2675.
[9] Ma H, Shi LL, Xu J, Li Y, Ma E. Appl Phys Lett 2005;87:181915.
[10] Jiang QK, Zhang GQ, Yang L, Wang XD, Saksl K, Franz H, et al. Acta Mater 2007;55:4409.
[11] Inoue A, Zhang W. Mater Trans 2004;45:584.

[12] Xu DH, Lohwongwatana B, Duan G, Johnson WL, Garland C. Acta Mater 2004;52:2621.
[13] Wang D, Li Y, Sun BB, Sui ML, Lu K, Ma E. Appl Phys Lett 2004;84:4029.
[14] Duan G, Xu DH, Johnson WL. Metal Mater Trans 2005;36A:455.
[15] Wang D, Tan H, Li Y. Acta Mater 2005;53:2969.
[16] Xu DH, Duan G, Johnson WL. Phys Rev Lett 2004;92:245504.
[17] Dai CL, Hua G, Yong S, Li Y, Ma E, Xu J. Scripta Mater 2006;54:1403.
[18] Jiang QK, Nie XP, Li YG, Jin Y, Chang ZY, Huang XM, et al. J Alloy Compds 2006;443:191.
[19] Han T, Zhang Y, Ma D, Feng YP, Li Y. Acta Mater 2003;51:4551.
[20] Jiang QK, Zhang GQ, Chen LY, Wu JZ, Zhang HG, Jiang JZ. J Alloy Compds 2006;424:183.
[21] Bouchard R, Hupfeld D, Lippmann T, Neuefeind J, Neumann HB, Poulsen HF, et al. Synchrotron Radiat 1998;5:90.
[22] Hammersley AP, Svensson SO, Hanfland M, Fitch AN, Häusermann D. High Press Res 1996;14:235.
[23] Yavari AR, Moulec AL, Inoue A, Nishiyama N, Lupu N, Matsubara E, et al. Acta Mater 2005;53:1611.
[24] Busch R, Kim YJ, Johnson WL. J Appl Phys 1995;77:4039.
[25] Jeong IK, Thompson J, Turner AMP, Billinge SJL. J Appl Crystallogr 2001;34:536.
[26] Zhang B, Wang RJ, Zhao DQ, Pan MX, Wang WH. Phys Rev B 2006;73:092201.
[27] Lee SW, Huh MY, Fleury E, Lee JC. Acta Mater 2006;54:349.
[28] Lu ZP, Liu CT. Acta Mater 2002;50:3501.
[29] Liu CT, Chisholm MF, Miller MK. Intermetallics 2002;10:1105.
[30] Castellero A, Bossuyt S, Stoica M, Deledda S, Eckert J, Chen GZ, et al. Scripta Mater 2006;55:87.
[31] Oh JC, Ohkubo T, Kim YC, Fleury E, Hono K. Scripta Mater 2005;53:165.
[32] Fan GJ, Freels M, Choo H, Liaw PK, Li JJZ, Rhim WK, et al. Appl Phys Lett 2006;89:241917.
[33] Liu L, Qiu CL, Zou H, Chan KC. J Alloy Compd 2005;399:144.
[34] Qin CL, Zhang W, Asami K, Kimura H, Wang XM, Inoue A. Acta Mater 2006;54:3713.
[35] Kissinger HE. Anal Chem 1957;29:1702.
[36] Miracle DB. Nat Mater 2004;3:697.
[37] Glade SC, Busch R, Lee DS, Johnson WL, Wunderlich RK, Fecht HJ. J Appl Phys 2000;87:7242.
[38] Angell CA. Science 1995;267:1924.
[39] Tanaka H. Phys Rev Lett 2003;90:055701.
[40] Mukherjee S, Schroers J, Zhou Z, Johnson WL, Rhim WK. Acta Mater 2004;52:3689.
[41] Lu ZP, Li Y, Liu CT. J Appl Phys 2003;93:286.
[42] Mukherjee S, Schroers J, Johnson WL, Rhim WK. Phys Rev Lett 2005;94:245501.
[43] Legg BA, Schroers J, Busch R. Acta Mater 2007;55:1109.
[44] Busch R, Schroers J, Wang WH. MRS Bull 2007;32:620.
[45] Miracle DB, Sanders WS, Senkov ON. Phil Mag A 2003;83:2409.
[46] Boer de FR, Boom R, Matterns WCM, Miedema AR, Niessen AK. Cohesion in metals. Amsterdam: North-Holland; 1998.
[47] Bruning R, Samwer K. Phys Rev B 1992;46:11318.